Experimental evidence of energy transfer and vibration mitigation in a vibro-impact acoustic black hole

Haiqin Li, Mathieu Sécail-Géraud, Adrien Pelat, François Gautier, Cyril Touzé

Experimental evidence of energy transfer and vibration mitigation in a vibro-impact acoustic black hole

Haiqin Li[a,b,*], Mathieu Sécail-Géraud[a], Adrien Pelat[a], François Gautier[a], Cyril Touzé[b]

[a] *Laboratoire d'Acoustique de l'Université du Mans, UMR CNRS 6613, Avenue Olivier Messiaen, 72085 Le Mans, Cedex 09, France*

[b] *IMSIA, ENSTA Paris-CNRS-EDF-CEA, Institut Polytechnique de Paris, 828 Boulevard des Maréchaux, 91762 Palaiseau Cedex, France*

Abstract

An experimental demonstration of the broadband passive damping capacity of a vibro-impact acoustic black hole (VI-ABH) is reported. A VI-ABH is an adaptation of the classical ABH design consisting of a beam with a tapered edge of decreasing thickness creating an acoustic black hole (ABH), complemented by contact points on which the beam impacts during its vibration. The contact nonlinearity creates a rapid and efficient transfer of vibrational energy from the low-frequency range, where the ABH is known to be ineffective, to the high-frequency range, thus improving the global passive vibration mitigation characteristics. The optimal design of a VI-ABH follows the rule of locating the contact points at local maxima of the low-frequency modes. Experiments clearly demonstrate the gain in performance, both in forced and free vibrations.

Keywords: Vibration mitigation; Acoustic Black Hole; Passive damping; Energy transfer; Vibro-impact nonlinearity

1. Introduction

Passive techniques to control unwanted vibrations represents an important field of research with numerous engineering applications. An attractive solution relies on the Acoustic Black Hole (ABH) effect, which attracts an increasing number of investigations in the recent past years [1–4]. The method relies on locally thinning the host structure following a power law and coating the inhomogeneous area with a visco-elastic layer so as incoming waves are efficiently trapped and damped out, above a threshold frequency [5, 6].

When considering its implementation on a beam, the ABH usually consists of manufacturing a wedge leading to a gradual decrease in celerity of any incoming flexural wave, and so a decrease in wavelength, making the dissipation due to the damping coating very efficient, even if only a small piece of damping material is used. Experimental evidence of such ABH effect has been reported in numerous publications, see *e.g.* [7–12] for direct observations on beams, plates and blades.

Although the ABH effect leads to very attractive damping efficiency in the mid to high frequency ranges - beyond a so-called *cut-on* frequency - , its damping capacity in the low-frequency range remains limited. Different analyses of the cut-on frequency have been pointed out, based on geometrical considerations [13, 14], following a phase point of view [15], from the analysis of dispersion relations [16], or in terms of localized modes [17]. In any case, the cut-on frequency represents the threshold frequency under which all the usual designs of ABH working on their linear regime do not lead to damping properties, due to the large typical wavelengths compared with the ABH characteristic length. However, in many engineering structures the vibration fields need to be mitigated using passive techniques in their low-frequency range.

Consequently, the idea of introducing some nonlinear effects in ABH dampers has recently emerged in order to improve the overall performance of the resulting devices. Indeed, a nonlinear characteristic is prone to transfer energy from low to high frequencies where the ABH is efficient, such that broadband vibration mitigation may be targeted by combining both effects.

First, geometric nonlinearity has been consid-

*Corresponding author.
Email address: lihaiqin1992@yahoo.com;Haiqin.Li@univ-lemans.fr (Haiqin Li)

ered in [18], showing a global improvement, limited by the long time scales of the energy transfer. Then, the use of contact nonlinearity has been numerically investigated in [19], in order to create a so-called Vibro-Impact ABH (VI-ABH), showing that the improvement can be significant with a very few contact points, well located at the local maxima of the low-frequency modes. Interestingly, analytical investigations of the energy redistribution caused by vibro-impact is the core of recent developments, shedding new light and giving theoretical foundations to the observed efficacy [20]. Other designs involving additional linear and/or nonlinear secondary absorber to control the low-frequency modes have also been numerically studied in [21].

Although the concept of VI-ABH has been numerically stated, to the best of our knowledge, no experimental proof has already been provided in order to demonstrate the gain in performance brought by the vibro-impact mechanism, as it is predicted in [19]. The aim of this paper is to report a complete experimental analysis of a VI-ABH beam demonstrator in order to state the advantages that this concept can reach in practice, as well as to provide guidelines for its design. The paper is organized as follows: The experimental setup is first introduced in section 2. In Section 3, both the permanent regime (forced vibrations) and transient dynamics (free vibrations) of the VI-ABH with one or several contact points are discussed. Section 4 contains concluding remarks of the main findings and a discussion of potential applications.

2. Experimental setup

The experimental setup is shown in Fig. 1. The ABH beam is made of inconel, manufactured with a 3D printed process with dimensions 460 mm × 20 mm × 3 mm, held vertically and clamped at its basis. The ABH wedge is 80 mm long and coated with an adhesive tape acting as the viscoelastic layer. The impactor is a solid steel tip that can be considered as perfectly rigid. It is mounted on a sliding system so that its vertical location is easy to set, as well as the gap with the beam, using a millimeter screw. When the impactor is set as desired, screws are stringly tightened so that it is rigidly clamped to the frame. The aluminum frame is oversized and arranged in order to ensure as rigid as possible contacts between the impactor and the beam, and so maximize the energy transfer, as recommended in the conclusions of the numerical study in [19].

Fig. 1(e) depicts the excitation and measuring devices. A shaker (LDS V201) fed by an amplifier (LDS PA25E) excites the beam at x_F=7.5 mm far from the beam clamp while an impedance head (PCB 288D01) captures the driving force and acceleration at the excitation point. A force sensor (PCB 208C03) placed at the impactor basis captures the contact force. A scanning laser vibrometer (PSV-500) is also used to measure the operating deflecting shapes of the beam when working in linear regime.

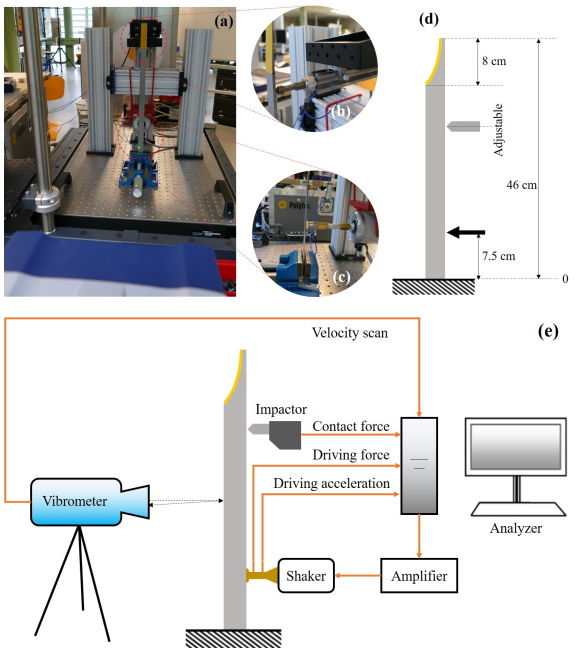

Fig. 1. (a): General picture of the experimental setup, and close-up views of (b): the impactor, (c): the clamped extremity of the beam and the shaker. (d): sketch of the set-up. (e): schematic view of the whole experimental apparatus.

3. Experimental results

3.1. Linear performance of the ABH

The linear behaviour of the tested ABH beam is first reported. The driving mobility with and without the damping layer is shown in Fig. 2(a). Over 250 Hz which corresponds to the cut-on frequency, the peaks of the transfer function of the linear ABH beam are strongly attenuated by 10 to 15 dB when the layer is placed. According to theoretical and numerical published background, Figs. 2(e-f) show that these peaks correspond to localized modes within the ABH wedge. However, the peaks of the first three modes are not attenuated and remain sharp, as expected. These modes

correspond in Fig. 2(b-d) to global modes of the clamped/free beam. Note that the very first mode at 12.5 Hz is not well captured due to the experimental setup limitations at so low frequency.

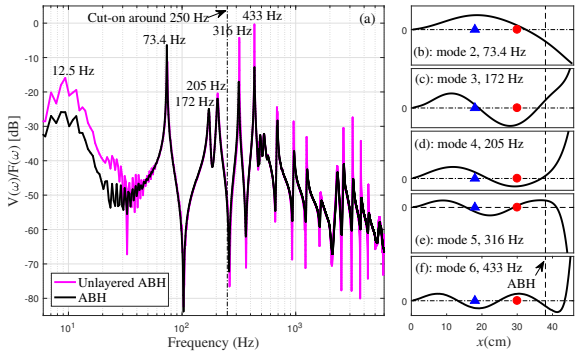

Fig. 2. (a): Driving mobility of the ABH beam with or without damping viscoelastic layer, (b-f): operational deflection shapes at selected frequencies corresponding to the peaks of the driving mobility.

3.2. Attenuation of low frequency peaks in forced regime

Based on the previous linear analysis, we target to attenuate the peaks of mode 2 at 73.4 Hz and mode 3 at 172 Hz, both being below the cut-on frequency at 250 Hz, by inserting the vibro-impacting device. Two contact point locations are considered in the following : The blue triangle on Fig. 2(b-d) indicates the location (at x_c=18 cm) of a local maximum of mode 2 which is also in the vicinity of a node of mode 3. Inversely, the red point at x_c=30 cm (see Fig. 2(b-d)) corresponds to a local maximum of mode 3 which is a node of mode 2.

Fig. 3 shows the results obtained when using a single contact point and exciting the beam in forced regime with a broadband white noise in the [5, 10000] Hz range. Fig. 3(a) plots the output spectrum of the driving velocity divided by the driving force spectrum, which would correspond to the driving mobility in the linear case without vibro-impact, and that is still used here for more straightforward comparison with Fig. 2. When placing a single contact point at x_c=18 cm (blue line), the peak of mode 2 is impressively attenuated by more than 25 dB while the peak of mode 3 is more slightly attenuated, as compared to the linear ABH case (black line). Inversely, mode 3 is strongly attenuated and mode 2 more slightly attenuated when placing the contact point at x_c=30 cm (red line). For both single contact locations, the energy transfer due to contact dynamics leads to a fuzzy spectrum at high frequencies, without resulting to an increase in peak amplitudes due to the ABH damping effect.

Next, combining the two previous cases leads to define a two-contact points configuration (green curve) in which both vibro-impactors at x_c=18 cm and x_c=30 cm are simultaneously used. The results show a cumulative effect leading to a strong attenuation of both modes 2 and 3. Note that either in the single and two-contact configurations, mode 4 is also attenuated, as the location of the involved impactors do not correspond to a node of mode 4. These observations agree very well with the numerical findings reported in [19, 21] showing the good predictive capacity of the previously published model.

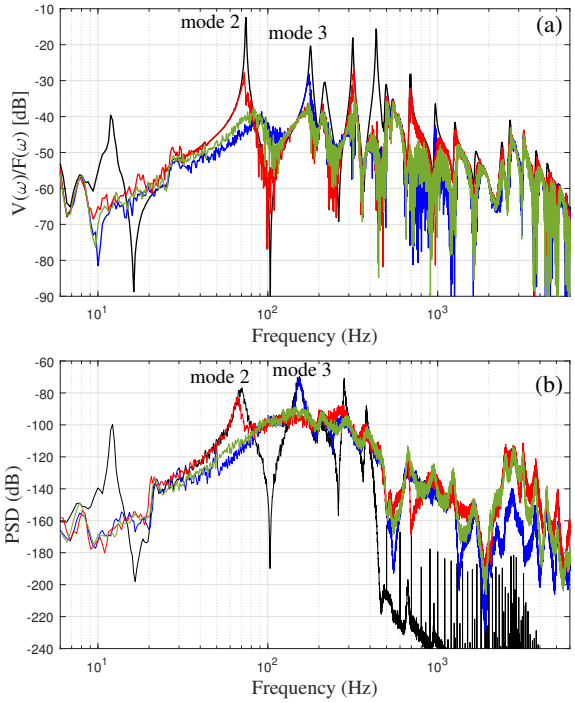

Fig. 3. (a): Spectrum of the driving velocity divided by the applied force, for a single contact point at x_c=30 cm (red), at x_c=18 cm (blue), for two contact points at both x_c=18 cm and x_c=30 cm (green), and for the non-contact case (black). This spectrum is the ABH beam response to a broadband white noise in the [5, 10000] Hz range applied at x_F=7.5 cm, (b): For the same four cases (i.e cases denoted by the same colors as (a)), comparison of the Power Spectrum Density of the beam velocity resulting from a low band white noise in the [5, 400] Hz range applied at x_F=7.5 cm.

In order to shed more light on the energy transfer and the related peak reduction brought by the VI-ABH, a noise excitation restricted to a low frequency range [5, 400] Hz is now considered. The power spectral density (PSD) of the velocity is displayed in Fig. 3(b) for the same four cases. The

spectra are computed from time signals acquired on 34 s using an average performed over short-time Fourier transforms of 3.2 s signals weighted by Hanning windows and with 50% overlap. In the $[5, 400]$ Hz range comprising the excitation frequencies, the same conclusions can be drawn as before. Above 400 Hz, the energy transfer is clearly highlighted by the increase in amplitude of the spectra that is associated with the peaks reduction below 400 Hz.

In order to evaluate more quantitatively the observed phenomena, a performance indicator denoted by I_Ω is introduced,

$$I_\Omega = 10\log_{10}\left[\frac{\int_\Omega P_v^{\text{cur}}(\omega)d\omega}{\int_\Omega P_v^{\text{ref}}(\omega)d\omega}\right], \qquad (1)$$

where $P_v^{\text{cur}}(\omega)$ and $P_v^{\text{ref}}(\omega)$ accounts for the PSD of the output velocity $v(x_F, t)$, and the superscript 'cur' and 'ref' respectively refer to the VI-ABH with contact (current case investigated) and to the reference case without contact (linear ABH). Ω denotes the frequency range of interest.

Considering the single contact VI-ABH case excited in the range [5,400] Hz, Fig. 4(a) plots the variations (in dB) of I_Ω with the contact point location when defining Ω=[5, 400] Hz (excitation frequency range, blue points), Ω=[400, 5000] Hz (high frequency range, red points), or Ω=[5, 5000] Hz (full frequency range, magenta points). For each of the 15 locations tested in the range x_c=18 cm to 38 cm, the average value of I_Ω (colored points) and its standard deviation (associated error bars) are estimated from 10 measurements.

For almost all contact point locations, Fig. 4(a) shows that the energy transfer leads to a significant reduction of the PSD at low frequency down to -10 dB for x_c=30 cm, giving rise to an increase at high frequencies of about 20 to 30 dB (keep in mind that this increase is relative to a negligible level of energy in the reference signal). As a matter of fact, indicators I_Ω computed in the low-frequency range ($[5, 400]$ Hz) and over the whole frequency band ($[5, 5000]$ Hz) are very close to each other, underlining that most of the energy is concentrated below 400 Hz, and that a general improvement of the mitigation is well achieved with the VI-ABH.

To go deeper and evaluate the mitigation efficiency mode by mode, Figs. 4(b-d) plot the indicators now calculated on narrow frequency ranges centered on the resonant frequencies of modes 2,3 and 5: I_{ω_2} is defined on [60,90] Hz for mode 2, I_{ω_3} in $[130, 220]$ Hz for mode 3, and I_{ω_5} in $[260, 320]$ Hz for mode 5. The trends of the gain in mitigation efficiency are shown to follow the shapes of

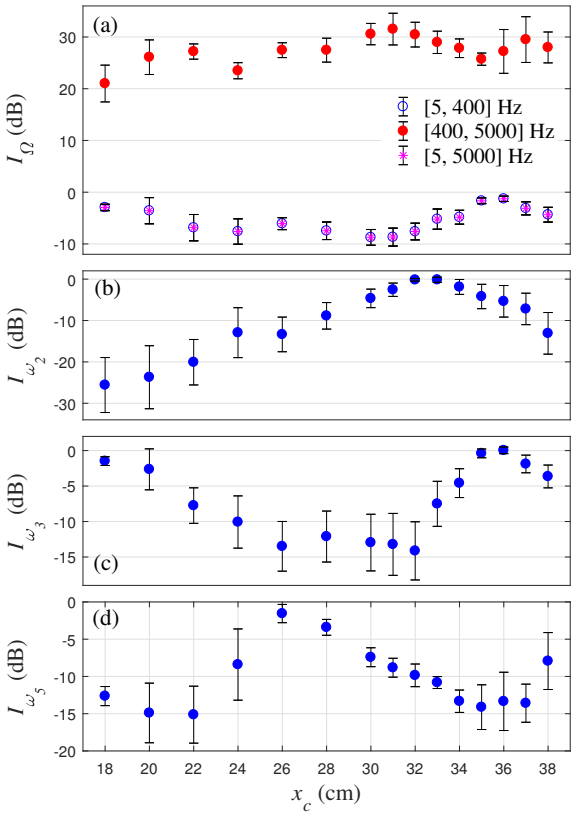

Fig. 4. (a): Indicators I_Ω calculated for the energy reduction at the low frequency range $[5, 400]$ Hz (blue), the energy transferred to the high frequency range $[400, 5000]$ Hz (red), and the whole band overall reduction $[5, 5000]$ Hz (magenta) . (b-d): Indicators calculated in the vicinity of the low frequency modes; I_{ω_2} for mode 2 at 73.4 Hz, I_{ω_3} for mode 3 at 172 Hz, and I_{ω_5} for mode 5 at 316 Hz. The contact point location varies from x_c=18 cm to x_c=38 cm. Measurements are repeated 10 times for each point, allowing reporting average value and standard deviation.

the eigenmodes in Figs. 2(b-c) and Fig. 2(e), confirming that the contact point location is the main control parameter enabling to select the mode to be mitigated.

3.3. Energy decay analysis in transient regime

The transient response resulting from a shock provided by an impact hammer (086C03) is now studied, aiming at evaluating the gains brought by vibro-impacts on the decay time of vibrational energy in the free regime. The impact is applied at x=25 cm approximately, while the velocity response of the beam is recorded by the laser vibrometer at x=7.5 cm, where the force has been applied by the shaker in the forced regime case. The input force pulse applied on the beam is plotted in Fig. 5(a), showing that the short contact

duration is approximately 4 ms, with a mean amplitude of 55 N (mean values found on 3 experiments). Therefore, the energy injected into the beam is large band and mostly concentrated in the range [0,3000] Hz (see Fig. 5(a)). One can also note that a double impact actually happens in Fig. 5(a), which is unfortunately unavoidable in real experimental situation due to the very short time scales provided by beam vibration and contact with impactor. Fig. 5(b) reports the transient signal measurements acquired for four different configurations. Two cases of ABH are first displayed, without (magenta curve) and with viscoelastic layer (black line). Then two cases of VI-ABH are shown, corresponding to a single contact point located at x_c=30 cm (red curve, only envelope shown) and x_c=18 cm (blue curve, full signal shown). For the first three cases, only the envelope curves are plotted for the sake of readability. For the considered excitation, the addition of the damping layer has a minor effect on the damping capacity of the ABH, with still important vibration amplitudes after 0.6 s. A strong improvement is reported for the VI-ABH cases, with for both cases a vibration totally damped out after 0.3 s. A slightly better damping capacity is observed for the last case (contact point at $x_c = 18$ cm).

To give a more quantitative understanding of the transient regime, an indicator representing the energy decay of the measured signals is introduced as

$$E_\sigma(\tau) = \frac{\int_\tau^{T_f} V^2\,\mathrm{d}t}{\int_0^{T_f} V^2\,\mathrm{d}t}, \quad \forall\,\tau \in [0,\ T_f], \qquad (2)$$

where V is the measured velocity of the beam. The energy decay E_σ is the ratio between the energy of the signal computed between the current time τ and the end of the signal window divided by the total energy of the signal. For $\tau = 0$, $E_\sigma = 1$, and the decrease of $E_\sigma(\tau)$ allows comparing the fastness of energy absorption in each measured configuration. Fig. 5(c) displays the energy decay of the four different cases analysed before. The effect of the damping layer is to slightly improve the decay slope: the vibrational energy is reduced by a factor of 100 after 420 ms, *i.e.* 30 ms faster than with uncoated ABH. This is due to the fact that the vibrational energy is mainly hold by the global low frequency modes for which the ABH is inefficient. On the other hand, for both VI-ABH cases, a much more steeper decay is obtained at the first instants of the vibration: the vibrational energy is reduced by a factor of 100 after 200 ms only, *i.e.* more than 200 ms faster than with the usual linear ABH. At larger time scales, the better performance of the case with the contact point

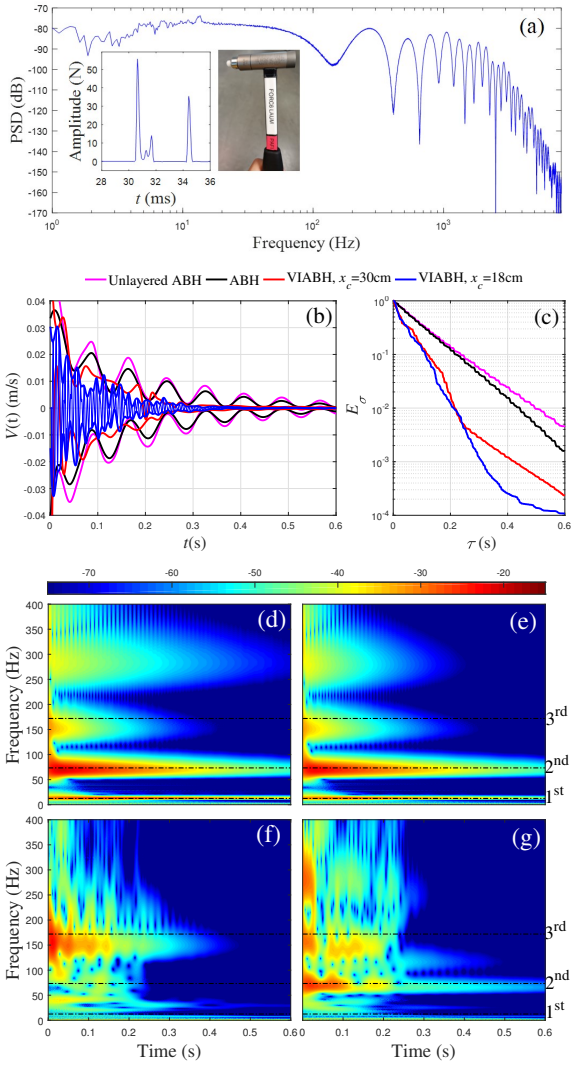

Fig. 5. (a): Typical frequency spectrum and associated time signal of the hammer impact force applied for the ABH transient analysis, (b): ABH beam velocity resulting from the impacting hammer : case of the ABH without vibro-impact and without damping layer (magenta curve), without vibro-impact and with damping layer (black curve). VI-ABH cases with one contact point (at $x_c = 30$ cm (red curve) and $x_c = 18$ cm (blue curve)). (c): energy decay $E_\sigma(\tau)$ for the four cases reported in (b). (d-g): Spectrograms of the ABH beam velocity for the four cases, with (d) unlayered ABH, (e) layered ABH, (f): VI-ABH with contact at x_c=18 cm, near the maximum of mode 2 (73 Hz) and node of mode 3 (172 Hz), and (g) VI-ABH with contact at x_c=30 cm, near the maximum of mode 3 and the node of mode 2.

at $x_c = 18$ cm is highlighted. Interestingly, the slope of the energy decay for the case $x_c = 30$ cm matches that of the layered ABH from τ=230 ms. This is interpreted by the fact that from this in-

stant, no contacts occurs anymore since the beam amplitude is small enough and the VI-ABH recovers its linear behaviour.

Figs. 5(d-g) show the spectrograms of the vibration of the four cases, centered in the low-frequency band [0,400] Hz in order to underline the time-frequency behaviour of the first three modes of the beam. Whereas the addition of the viscoelastic layer only shows a small effect above the cut-on frequency, the changes brought by adding a contact point are drastic with energy transfers to higher frequencies and appearance of a more complex and erratic spectrum. The most striking difference between the two VI-ABH cases, Figs. 5(f-g), is the control of the second eigenfrequency, which is much more effective for the case in Fig. 5(f) where the contact point is at $x_c = 18$ cm, underlining again the importance of the contact point location with respect to eigenmode shape maxima. In any case, this study of the VI-ABH performance in the transient regime experimentally demonstrates the efficiency of the device to rapidly damp out free vibrations.

4. Conclusion

An experimental evidence of the effectiveness of a VI-ABH has been reported. The device combines the important damping capacity of the ABH over its cut-on frequency, to a contact nonlinearity, allowing redistribution of energy among all frequencies in order to improve the overall damping capacity. The resulting effect of the vibro-impact is to wipe out the sharp resonance peaks below the cut-on frequency and efficiently transfer their vibratory energy to higher frequencies where they are mitigated by the ABH effect. Experiments on an ABH beam have been investigated, both in forced and free vibrations. The location of the contact point has been shown to follow the rule of eigenmode maxima for optimal performance of control of low-frequency modes, confirming the numerical findings reported in [19], and thus offering a simple yet efficient design strategy that can be used for more complex ABH devices such as *e.g.* plates with elliptical or networks of tapered regions. It is worth underlining that VI-ABH appears as a very efficient technique for vibration mitigation, and the amount of energy transferred to air via acoustic coupling and sound radiation is negligible as compared to vibratory energy. Nevertheless, the sound produced by the device is more important than the more silent standard ABH, such that this might lead to restricting the applicability of VI-ABH to contexts where noise annoyance is not a critical point, space industry being such an example.

References

[1] V. V. Krylov. Acoustic black holes: recent developments in the theory and applications. *IEEE Transactions on Ultrasonics, Ferroelectrics, and Frequency Control*, 61(8):1296–1306, 2014.

[2] A. Pelat, F.Gautier, S.C. Conlon, and F. Semperlotti. The acoustic black hole: A review of theory and applications. *Journal of Sound and Vibration*, 476:115316, 2020.

[3] C. Zhao and M. Prasad. Acoustic black holes in structural design for vibration and noise control. *Acoustics*, 1(1):220–251, 2019.

[4] J. Deng, O. Guasch, L. Maxit, and L. Zheng. Reduction of bloch-floquet bending waves via annular acoustic black holes in periodically supported cylindrical shell structures. *Applied Acoustics*, 169:107424, 2020.

[5] V.V. Krylov and F.J.B.S. Tilman. Acoustic 'black holes' for flexural waves as effective vibration dampers. *Journal of Sound and Vibration*, 274(3-5):605–619, 2004.

[6] N. Gao, Z. Wei, R. Zhang, and H. Hou. Low-frequency elastic wave attenuation in a composite acoustic black hole beam. *Applied Acoustics*, 154:68–76, 2019.

[7] V.V. Krylov and R.E.T.B. Winward. Experimental investigation of the acoustic black hole effect for flexural waves in tapered plates. *Journal of Sound and Vibration*, 300(1-2):43–49, 2007.

[8] D.J. O'Boy, V.V. Krylov, and V. Kralovic. Damping of flexural vibrations in rectangular plates using the acoustic black hole effect. *Journal of Sound and Vibration*, 329(22):4672–4688, 2010.

[9] V. Denis, F. Gautier, A. Pelat, and J. Poittevin. Measurement and modelling of the reflection coefficient of an acoustic black hole termination. *Journal of Sound and Vibration*, 349:67–79, 2015.

[10] E.P. Bowyer, D.J. O'Boy, V.V. Krylov, and F. Gautier. Experimental investigation of damping flexural vibrations in plates containing tapered indentations of power-law profile. *Applied Acoustics*, 74(4):553–560, 2013.

[11] P.A. Feurtado and S.C. Conlon. An experimental investigation of acoustic black hole dynamics at low, mid, and high frequencies. *Journal of Vibration and Acoustics*, 138(6):061002, 2016.

[12] E.P. Bowyer and V.V. Krylov. Damping of flexural vibrations in turbofan blades using the acoustic black hole effect. *Applied Acoustics*, 76:359–365, 2014.

[13] V. Denis, A. Pelat, and F. Gautier. Scattering effects induced by imperfections on an acoustic black hole placed at a structural waveguide termination. *Journal of Sound and Vibration*, 362:56 – 71, 2016.

[14] S.C. Conlon, J.B. Fahnline, and F. Semperlotti. Numerical analysis of the vibroacoustic properties of plates with embedded grids of acoustic black holes. *The Journal of the Acoustical Society of America*, 137(1):447–457, 2015.

[15] S.C. Conlon and P.A. Feurtado. Progressive phase trends in plates with embedded acoustic black holes. *The Journal of the Acoustical Society of America*, 143(2):921–930, 2018.

[16] O. Aklouche, A. Pelat, S. Maugeais, and F. Gautier. Scattering of flexural waves by a pit of quadratic profile inserted in an infinite thin plate. *Journal of Sound and Vibration*, 375:38–52, 2016.

[17] J. Leng, V. Romero-García, A. Pelat, R. Picó, J-P. Groby, and F. Gautier. Interpretation of the acoustic black hole effect based on the concept of critical coupling. *Journal of Sound and Vibration*, page 115199, 2020.

[18] V. Denis, A. Pelat, C. Touzé, and F. Gautier. Improvement of the acoustic black hole effect by using energy transfer due to geometric nonlinearity. *International Journal of Non-Linear Mechanics*, 94:134–145, 2017.

[19] H. Li, C. Touzé, A. Pelat, F. Gautier, and X. Kong. A vibro-impact acoustic black hole for passive damping of flexural beam vibrations. *Journal of Sound and Vibration*, 450:28–46, 2019.

[20] M. Gzal, B. Fang, A. F. Vakakis, L. A. Bergman, and O. V. Gendelman. Rapid non-resonant intermodal targeted energy transfer (imtet) caused by vibro-impact nonlinearity. *Nonlinear Dynamics*, 101(4):2087–2106, 2020.

[21] H. Li, C. Touzé, A. Pelat, and F. Gautier. Combining nonlinear vibration absorbers and the acoustic black hole for passive broadband flexural vibration mitigation. *International Journal of Non-Linear Mechanics*, page 103558, 2020.